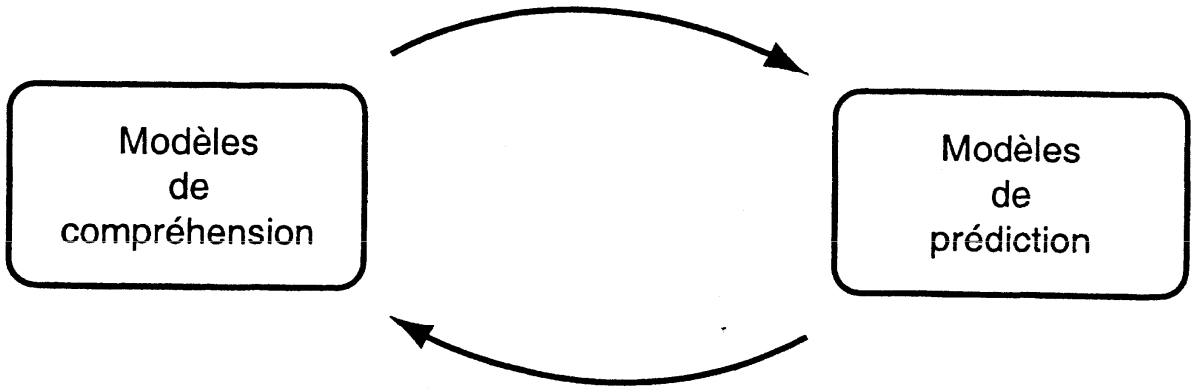

FIG. 1.5 – *Les deux grandes familles de modèles.*

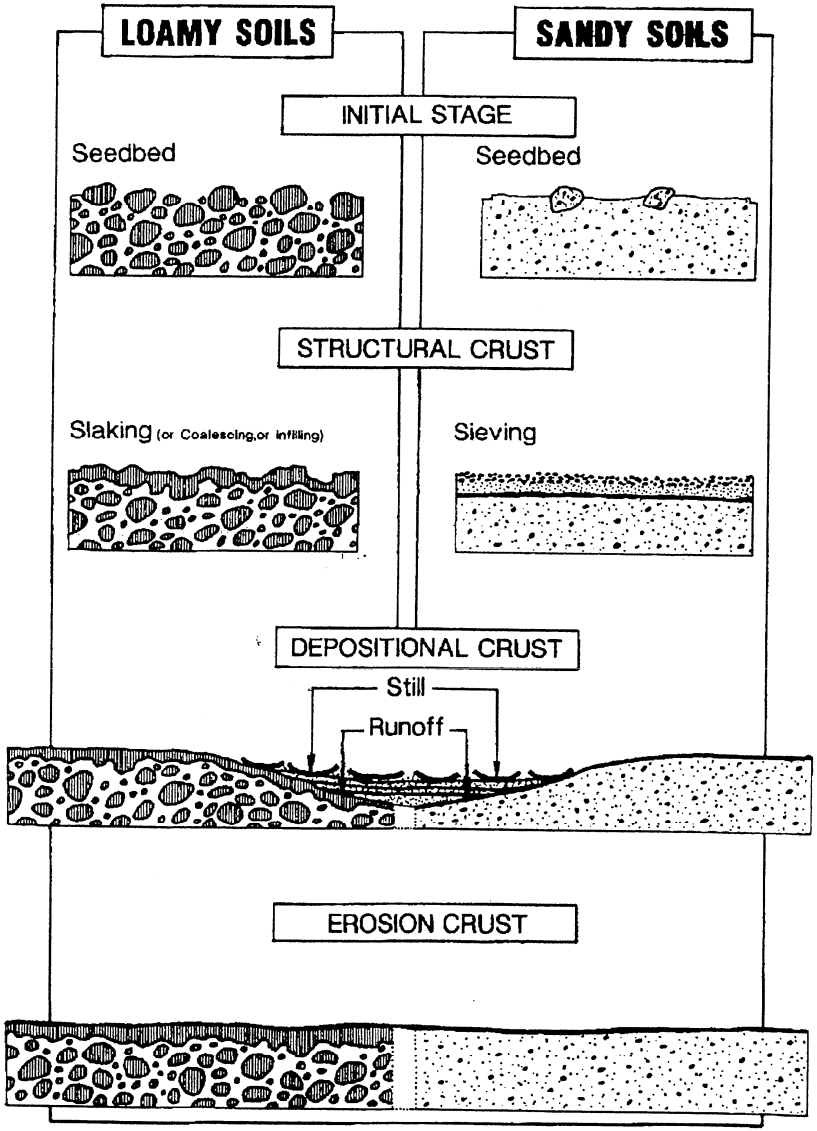

FIG. 1.2 – *Évolution des états de surfaces.*
Partant d'un lit de semences (sol limoneux à gauche, sol sablonneux à droite), les précipitations et le ruissellement vont faire apparaître différentes croûtes en surface. Extrait de Valentin et Bresson (1992).

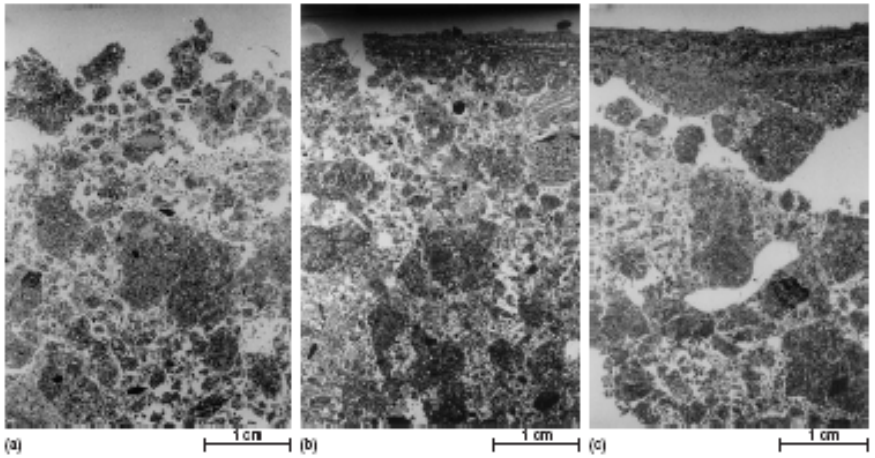

Figure 1 Vertically oriented thin section from samples of the 0–6 cm soil layer: (a) before the rain simulation – a crumbly to subangular blocky structure is evident; (b) after 22 mm rain – the presence of a surface seal is visible; (c) after 71 mm rain. Pictures were taken at ×2 magnification under plain polarized light (parallel Nicols, pores appear white).

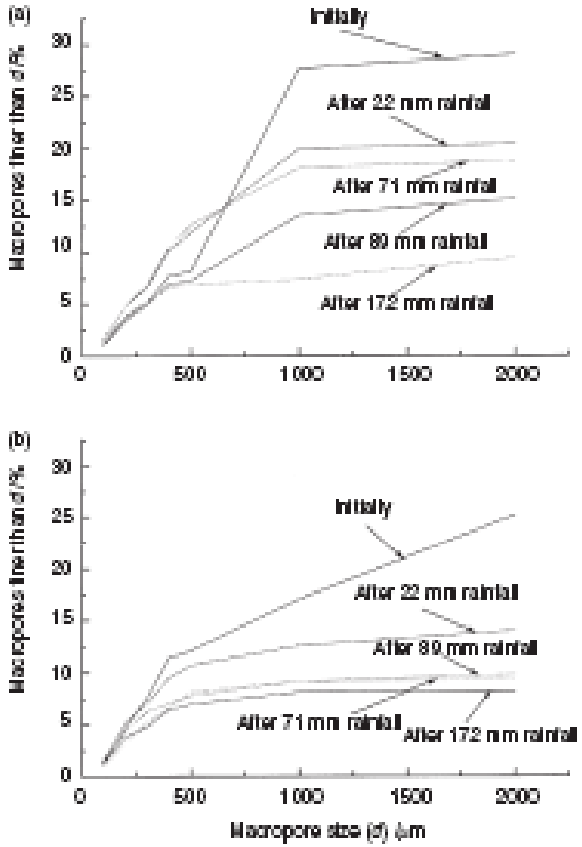

Figure 4 Cumulative pore-size distributions obtained by image analysis of thin sections from samples of (a) the S-layer (0–3 cm) and (b) the U-layer (3–6 cm) at four consecutive time intervals during the simulated rain (respective cumulative rain rates are shown).

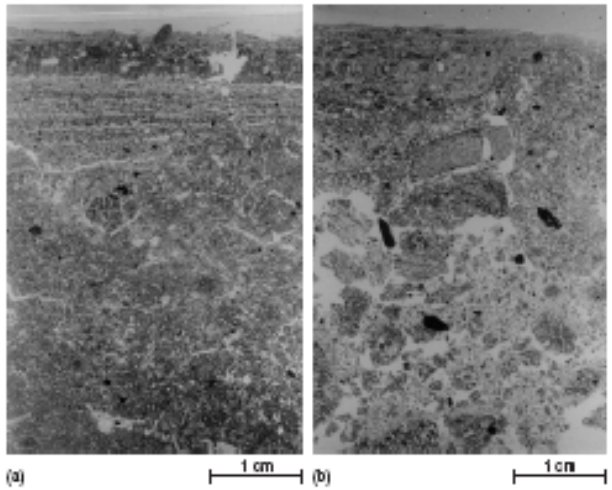

Figure 2 Vertically oriented thin section from samples of the 0–6 cm soil layer after 172 mm rain: (a) depositional seal; (b) structural seal. Pictures were taken at ×2 magnification under plain polarized light (parallel Nicols).

Rousseva et al. (2002) Effect of rain on macroporosity at the soil surface

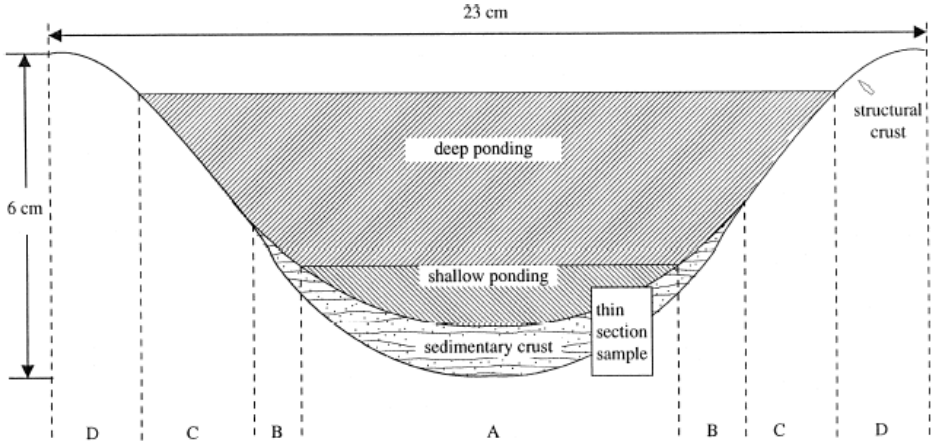

Fig. 1. Schematic representation of soil surface depression showing the approximate configuration of the sedimentary and structural crusts and the location of the thin section samples.

Fox et al (1998) The effect of ponding on infiltration in a crusted surface depression

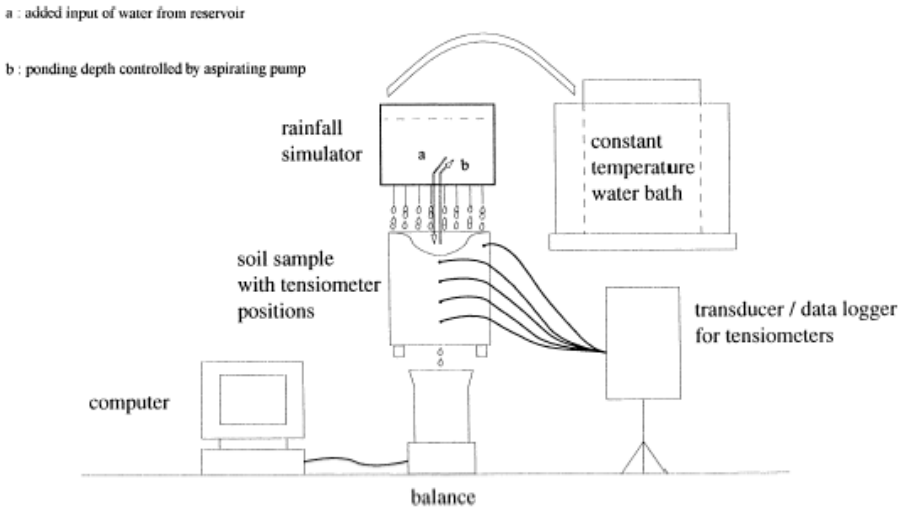

Fig. 2. Experimental setup: water at constant temperature was supplied to the rainfall simulator and directly into the depression under deep ponding. Ponding depth was controlled by an aspirator pump, and the water flux was measured continuously.

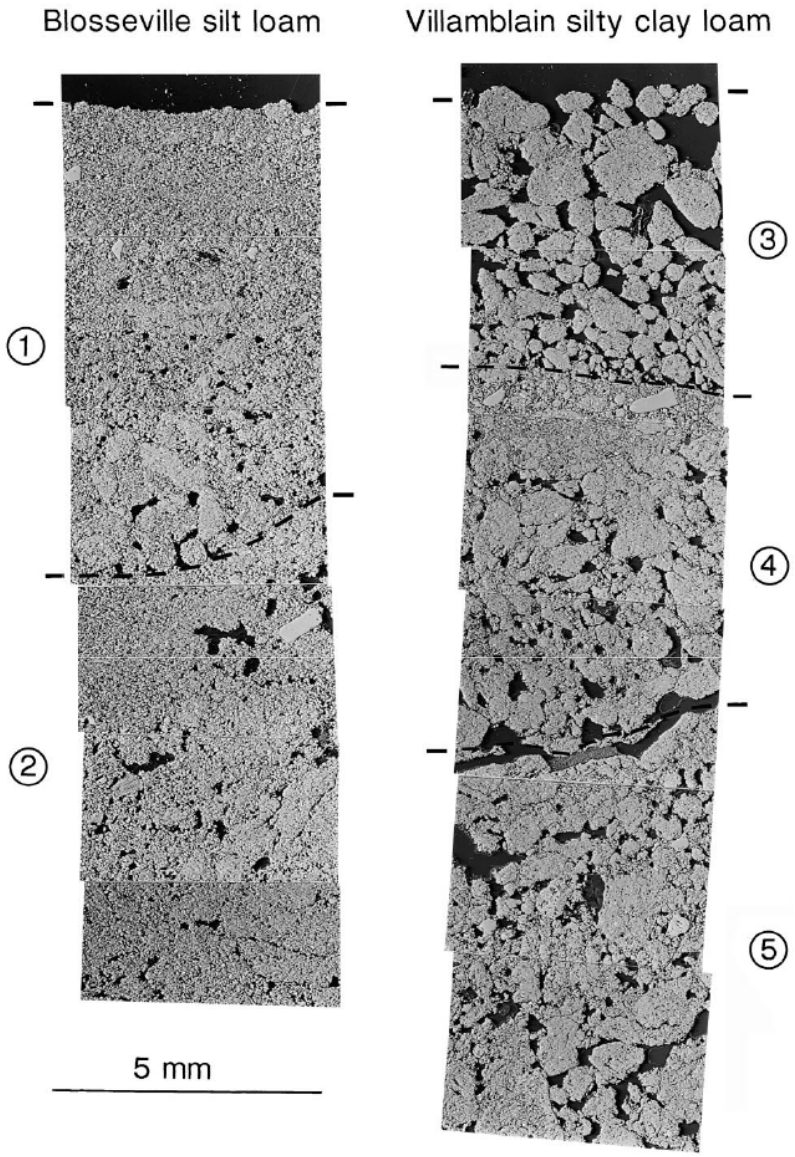

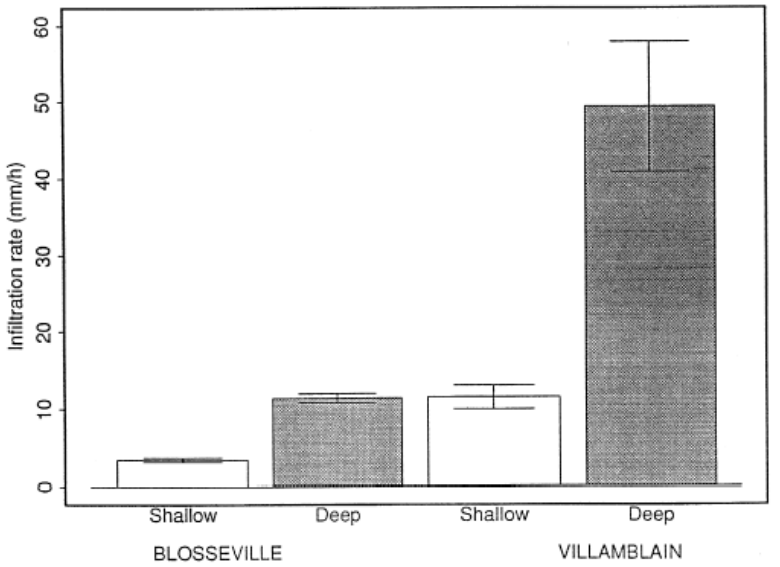

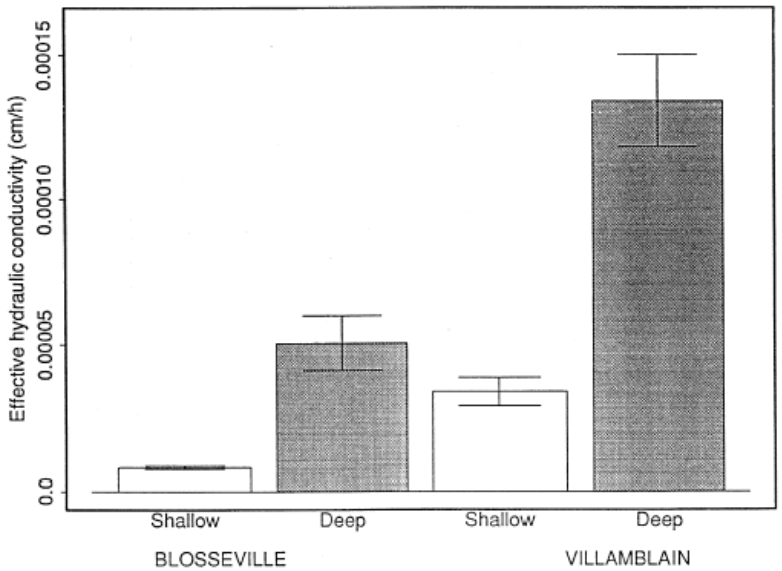

Fig. 3. Backscattered Electron Scattering Images (BESI) of crust sections (sample locations shown in Fig. 1). 1—Sedimentary crust with, at the base, close packing of remaining initial aggregates with disaggregated material. 2—Collapsed structure of initial soil with few remaining aggregates. 3—Depression infilling with detached aggregates. 4—Sedimentary crust with at the bottom a loose packing of initial aggregates. 5—Initial soil structure with numerous initial aggregates in loose packing.

Fox et al (1998) The implications of spatial variability in surface seal hydraulic resistance for infiltration in a mound and depression microtopography

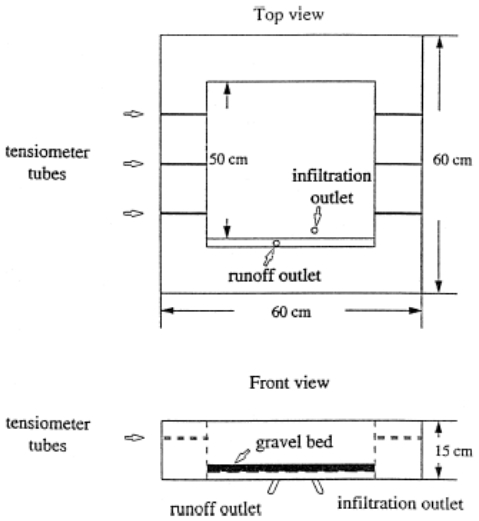

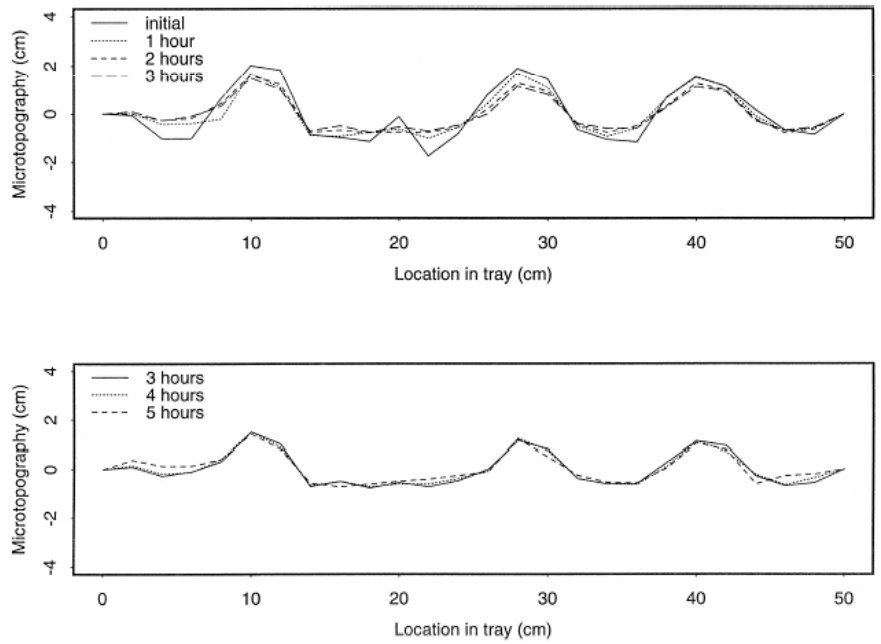

Fig. 2. Changes in microtopography for Blosseville showing the progressive flattening of the surface with time (a) during first 3 h rainfall simulation, (b) during final 2 h rainfall simulation.

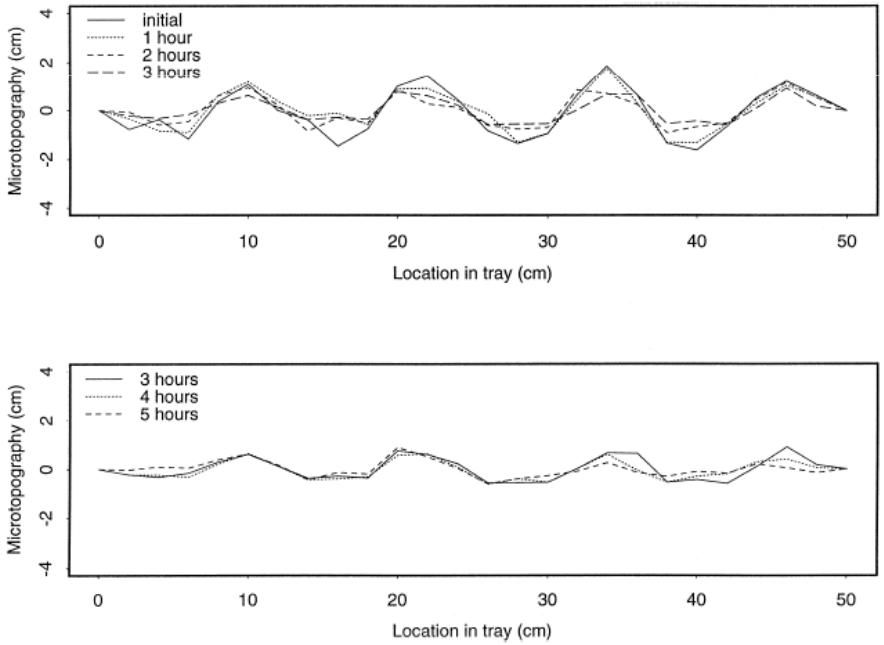

Fig. 3. Change in microtopography for Villamblain showing the progressive flattening of the surface with time (a) during first 3 h rainfall simulation, (b) during final 2 h rainfall simulation.

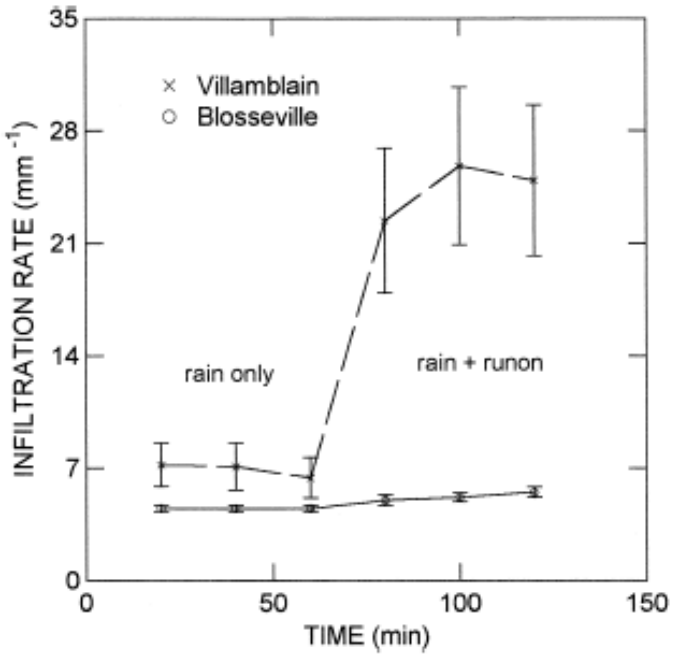

Table 1
Changes in ponded depth, pressure head, and infiltration rate with added runon and predicted infiltration rates from Eqs. (4) and (5) (values in parenthesis are standard errors)

Soil	Ponding treatment	Ponded depth (mm)	Pressure head (cm)	Infiltration rate (mm h^{-1})	Predicted infiltration rate (mm h^{-1})
Blosseville	Shallow	1.21 (0.34)	−6.80 (0.47)	4.36 (0.18)	8.8
	Deep	2.38 (0.46)	−6.24 (0.38)	5.66 (0.35)	7.5
Villamblain	Shallow	1.02 (0.22)	−9.96 (0.55)	6.60 (1.36)	25.2
	Deep	2.32 (0.21)	−8.36 (0.53)	25.4 (4.71)	43.3

Table 2
Hydraulic resistance values for both seal and soil types (values in brackets are standard errors)

Soil	Seal type	Hydraulic resistance (h)
Villamblain	Structural	0.53 (0.05)
	Depositional	3.40 (0.71)
Blosseville	Structural	5.90 (0.23)
	Depositional	33.2 (5.50)

Espessura da crosta/condutividade hidráulica da crosta

Rugosidade

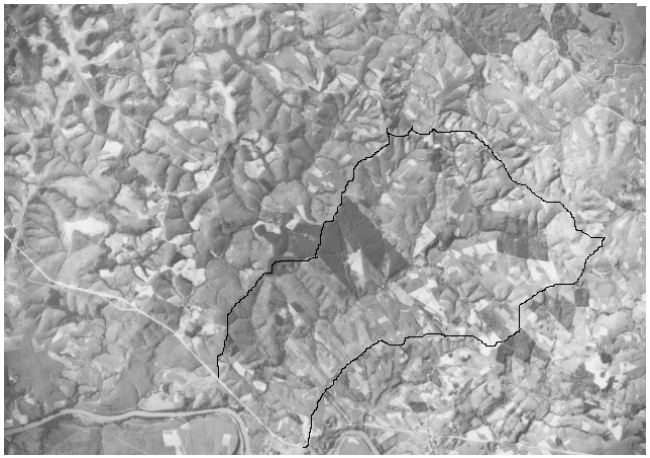

Relevo

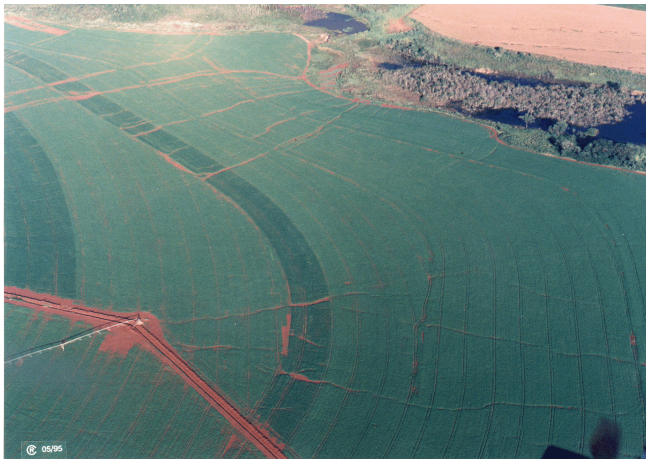

Rugosidade orientada

Rugosidade aleatória

Processo de formação da enxurrada

Coef de enxurrada = quantidade de água perdida pela enxurrada / volume da precipitação

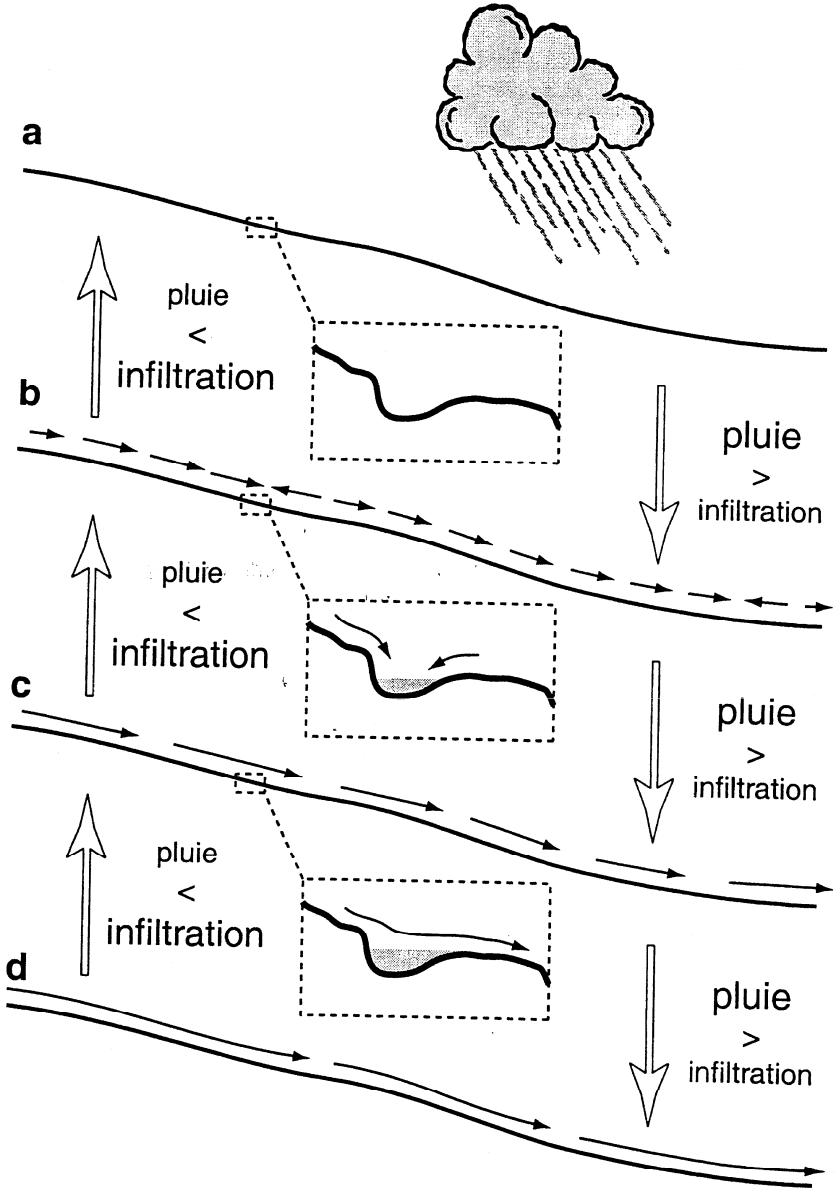

FIG. 1.3 – *Évolution des transferts d'eau au cours d'une averse. Les transferts par ruissellement sont schématisés par les flèches parallèles au profil topographique (leurs longueurs se veulent proportionnelles à la distance de parcours). Le détail de la surface montre le cas particulier d'une dépression.*

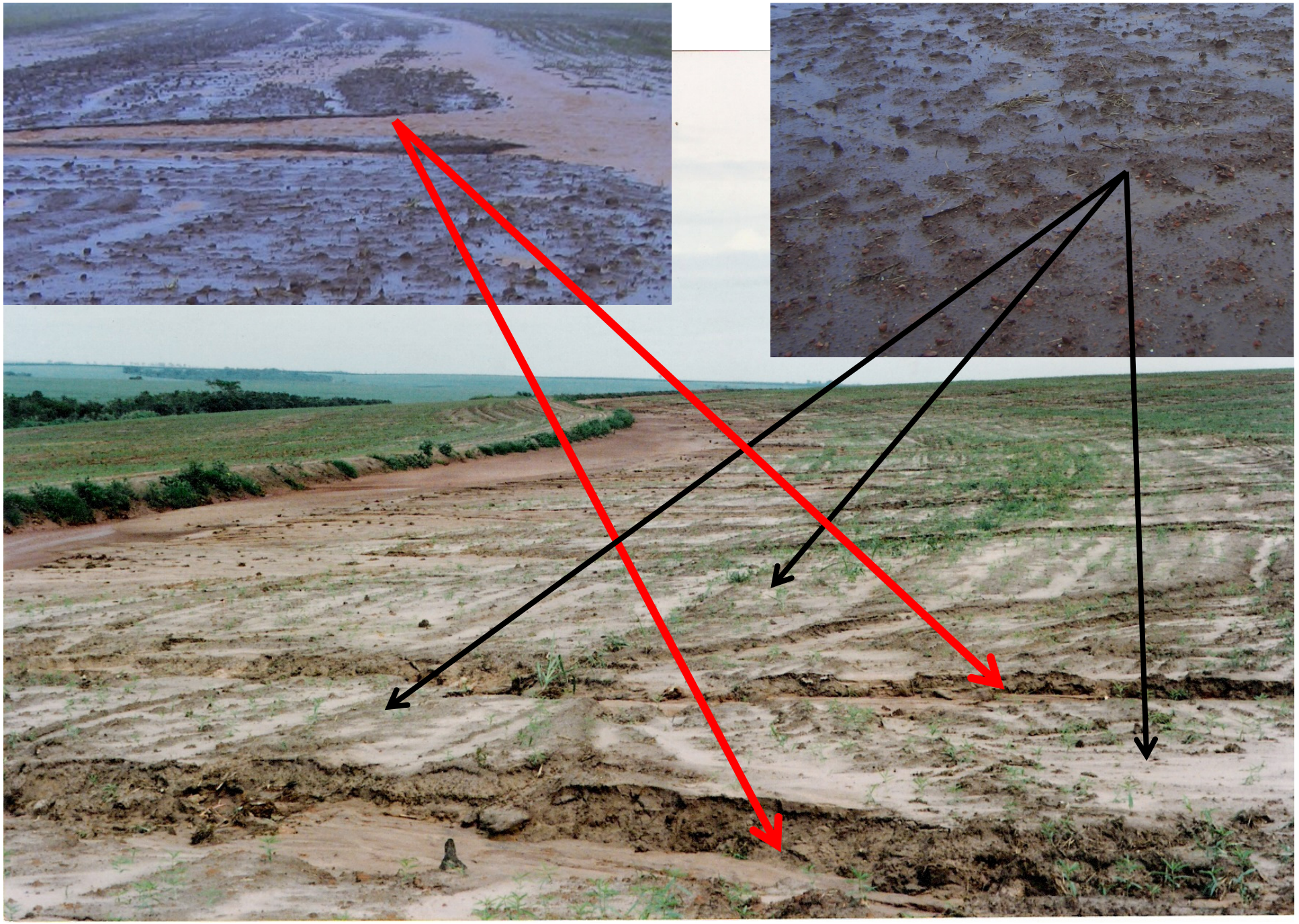

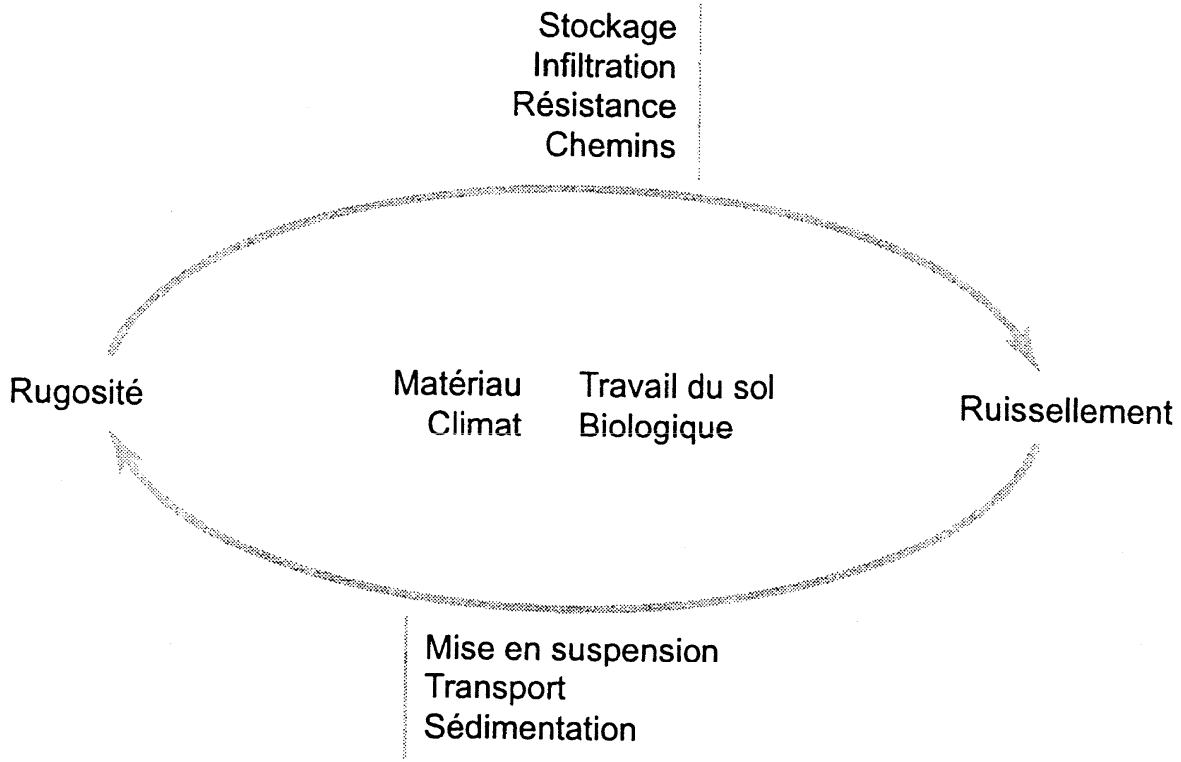

FIG. 1.4 – *Schéma simplifié des interactions entre rugosité et ruissellement.*

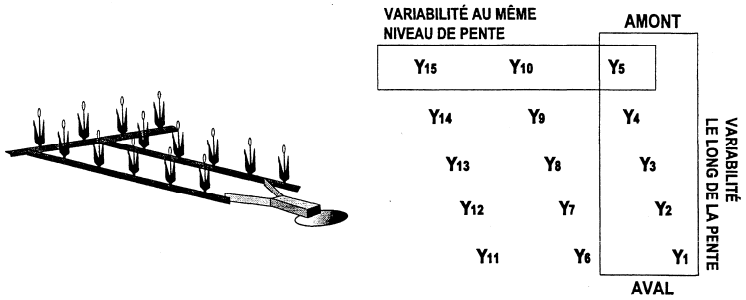

FIG. 1.6 – *Méthode d'étude de la variabilité spatiale du ruissellement.*
(a) Schéma d'implantation du dispositif de collecte du ruissellement.
(b) Répartition spatiale des dispositifs de mesure.
D'après Cros-Cayot (1996).

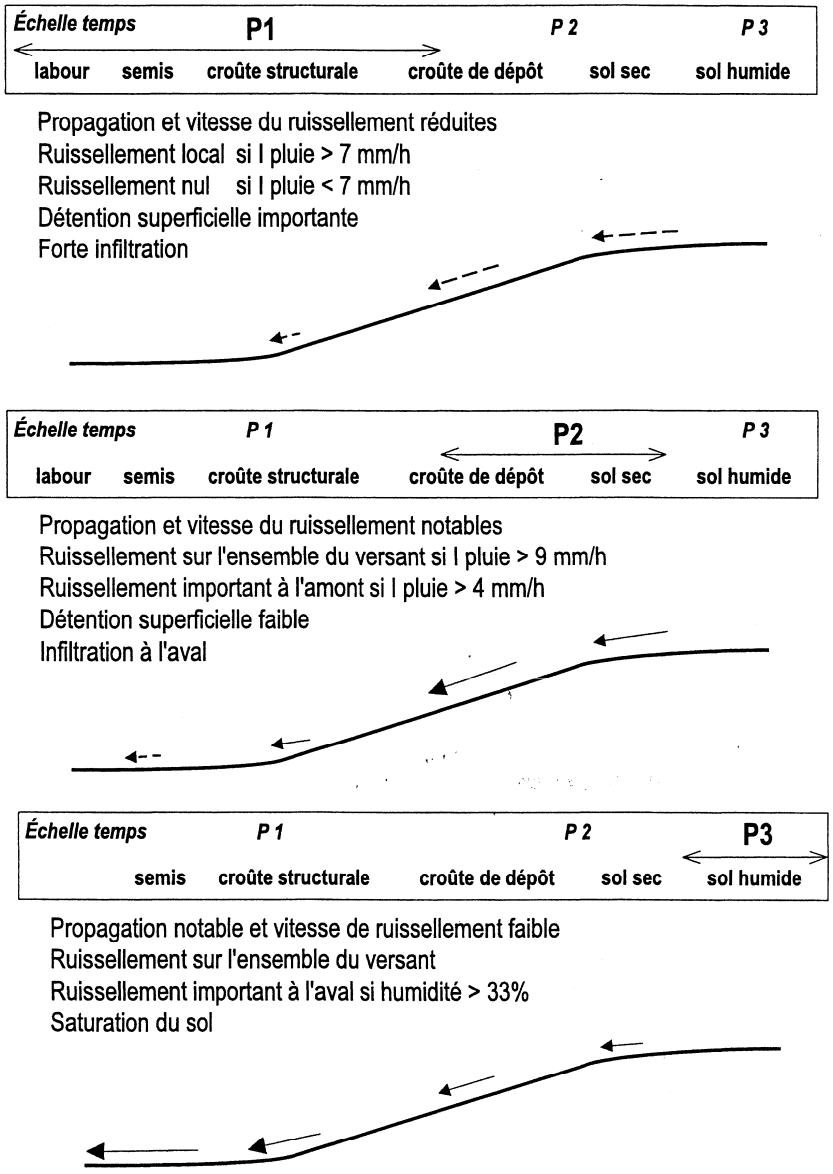

FIG. 1.7 – *Caractérisation des transferts d'eau par ruissellement sur une parcelle en contexte breton.*
Les propriétés du ruissellement varient au cours de l'année.
D'après Cros-Cayot (1996).

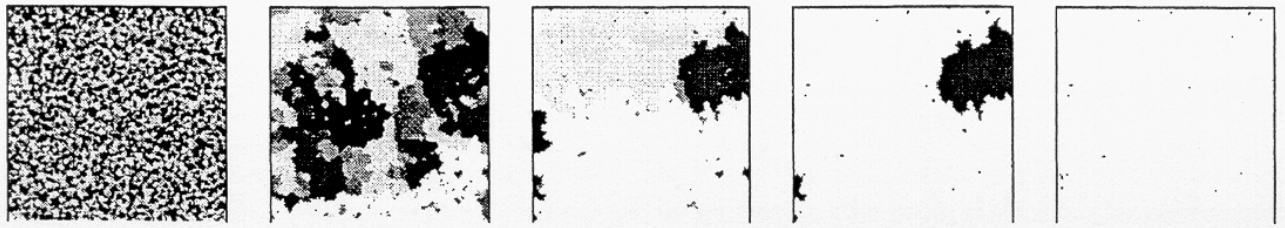

Figure 3.3: Evolution of drained areas during overland flow triggering without infiltration.
The closed boundaries are in black. The drained area contributing to runoff is in white. Unconnected drained areas are distinguished using grey levels.

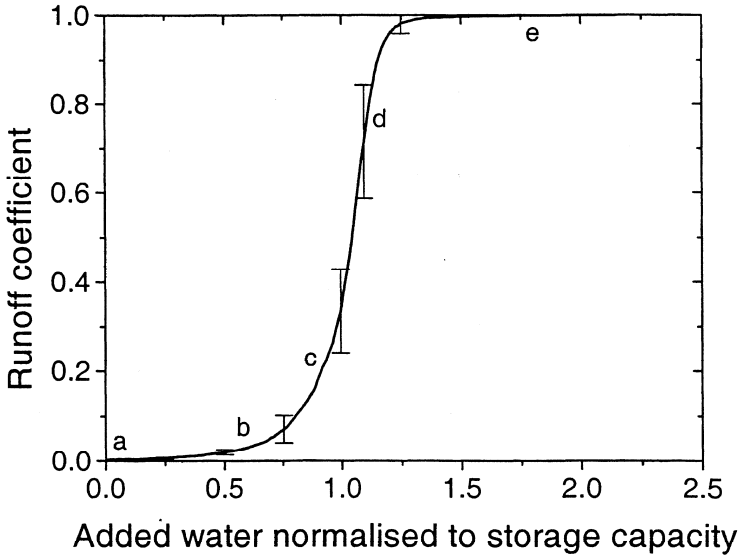

Figure 3.5: Evolution of runoff coefficient.

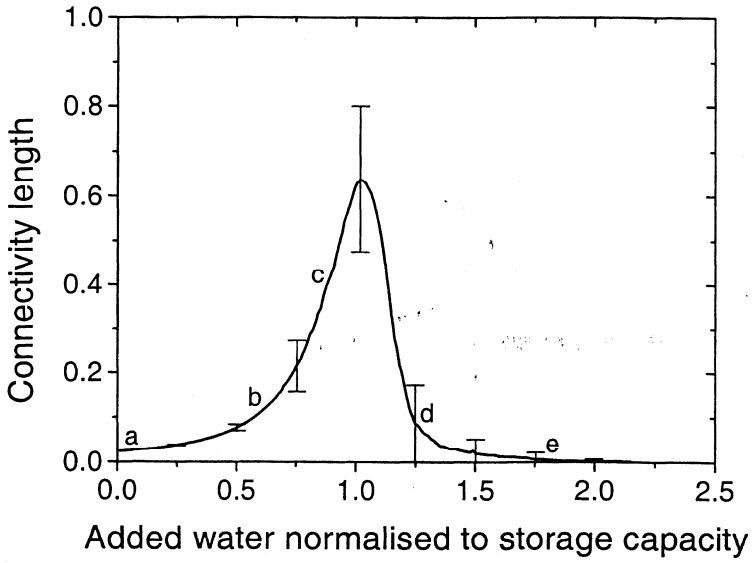

Figure 3.7: Evolution of connectivity length.

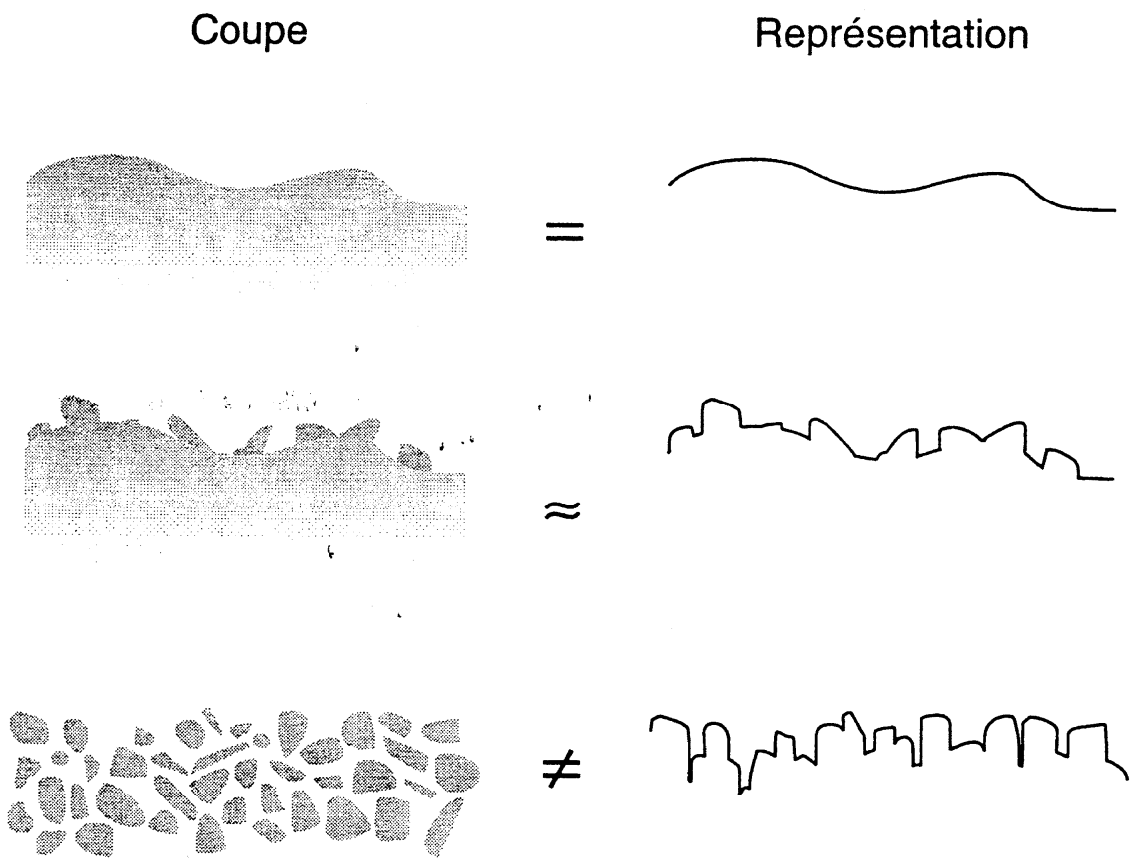

FIG. 4.1 – *Profils de surface de sol : coupes et représentations.*
Les méthodes de mesure utilisées exercent des contraintes fortes sur la représentation géométrique. En particulier, elles obligent à ne considérer qu'une seule altitude sur chaque verticale du profil.

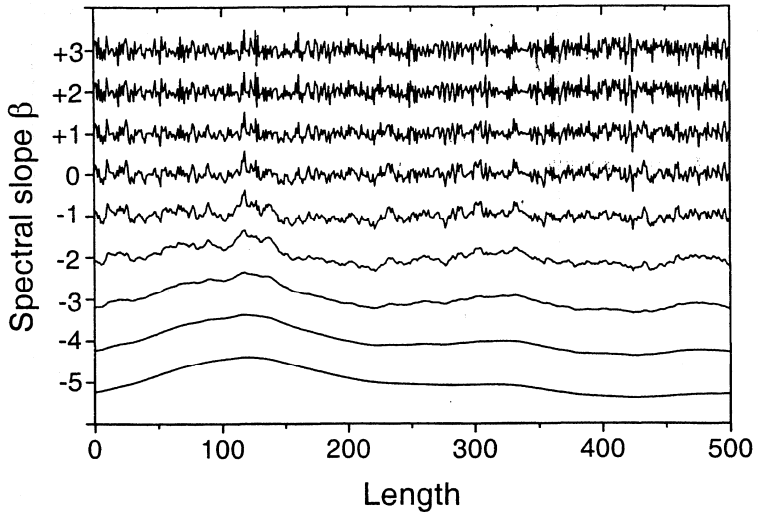

Figure 4.2: Cross-sections of generated surfaces depending on spectral slope β. Cross-sections are correlated for $\beta < 0$, uncorrelated for $\beta = 0$ and anti-correlated for $\beta > 0$.

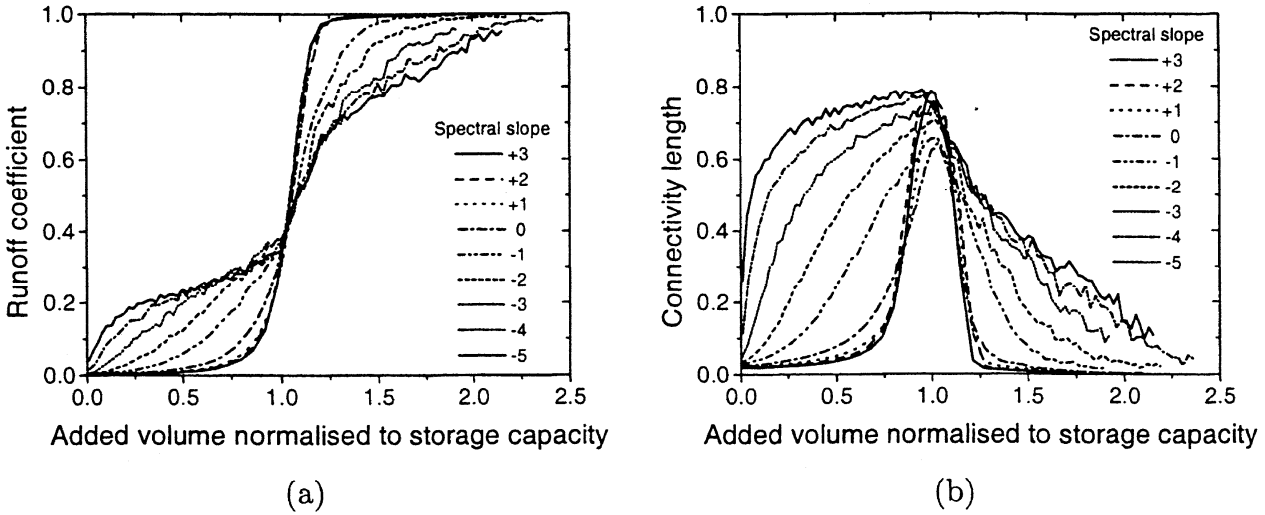

Figure 4.3: Runoff coefficient (a) and connectivity length (b) depending on spectral slope.

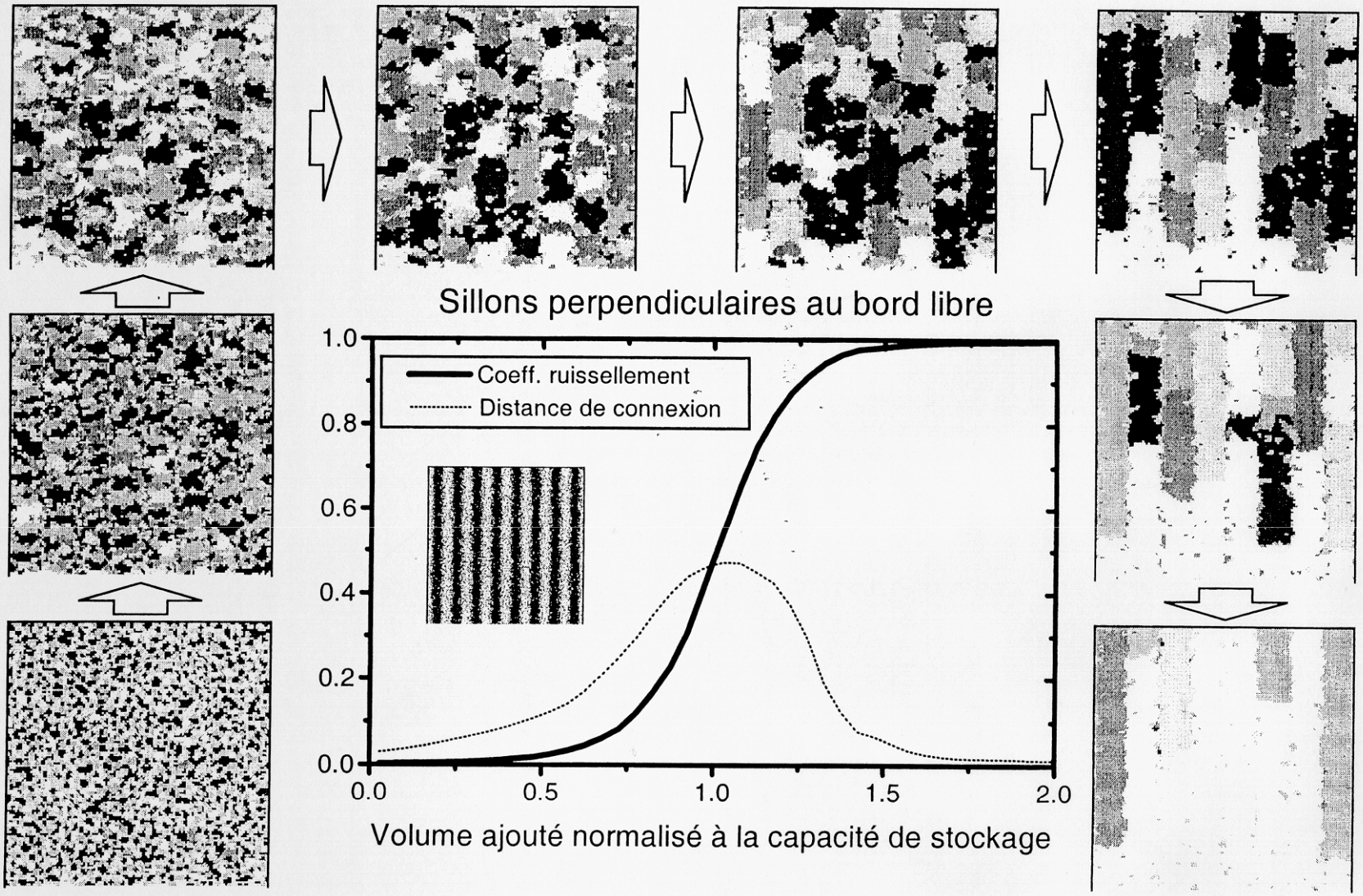

FIG. 4.10 – *Un exemple d'évolution de la géométrie des aires drainées dans le cas de sillons perpendiculaires au bord ouvert. L'amplitude des sillons est de 2 ; la pente générale est nulle. Les bords fermés sont en noir, l'aire drainée connectée au bord ouvert est en blanc, les aires drainées non connectées sont en niveaux de gris. Les courbes sont une moyenne sur cent réalisations.*

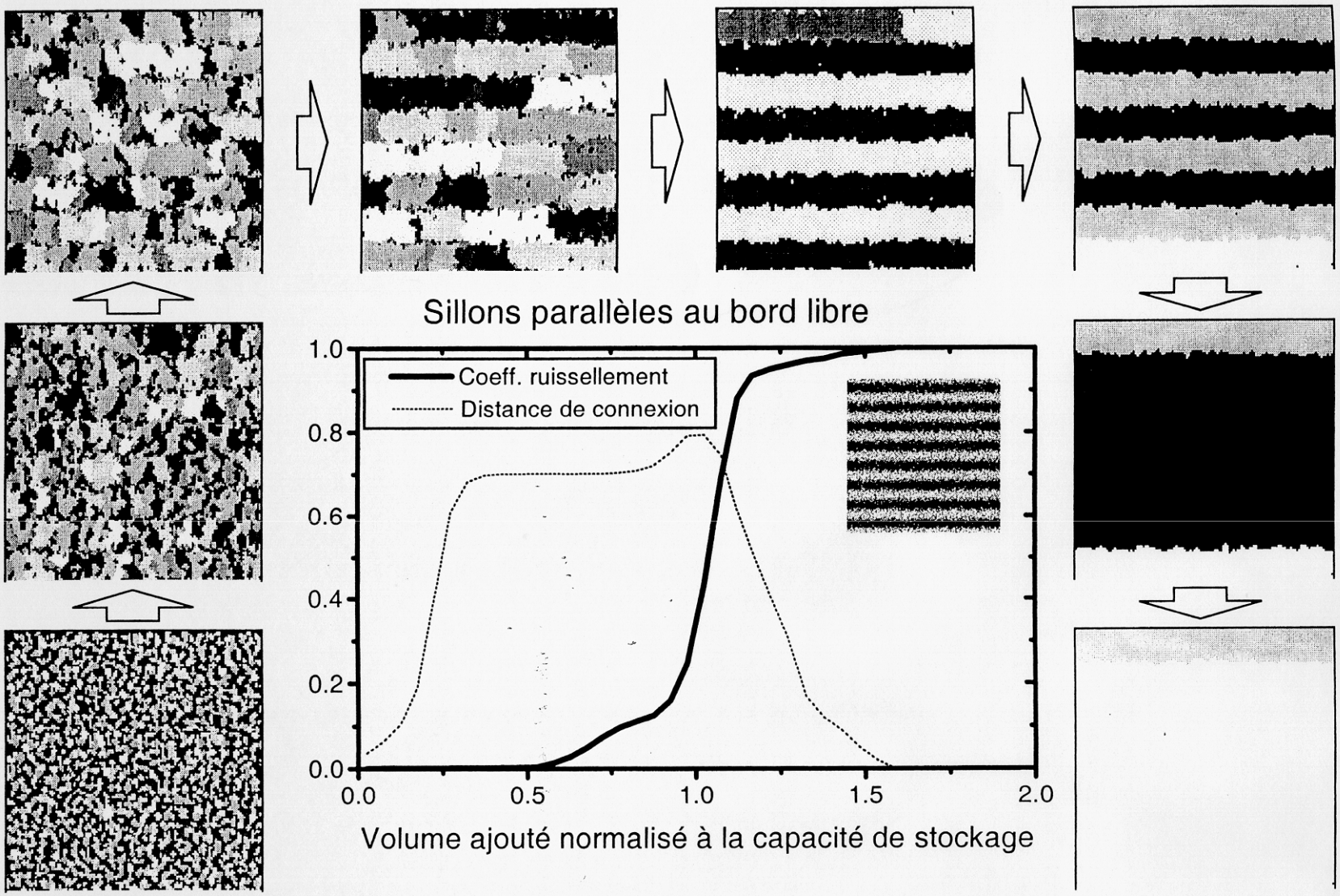

FIG. 4.11 – *Un exemple d'évolution de la géométrie des aires drainées dans le cas de sillons parallèles au bord ouvert. L'amplitude des sillons est de 2 ; la pente générale est nulle. Les bords fermés sont en noir, l'aire drainée connectée au bord ouvert est en blanc, les aires drainées non connectées sont en niveaux de gris. Les courbes sont une moyenne sur cent réalisations.*

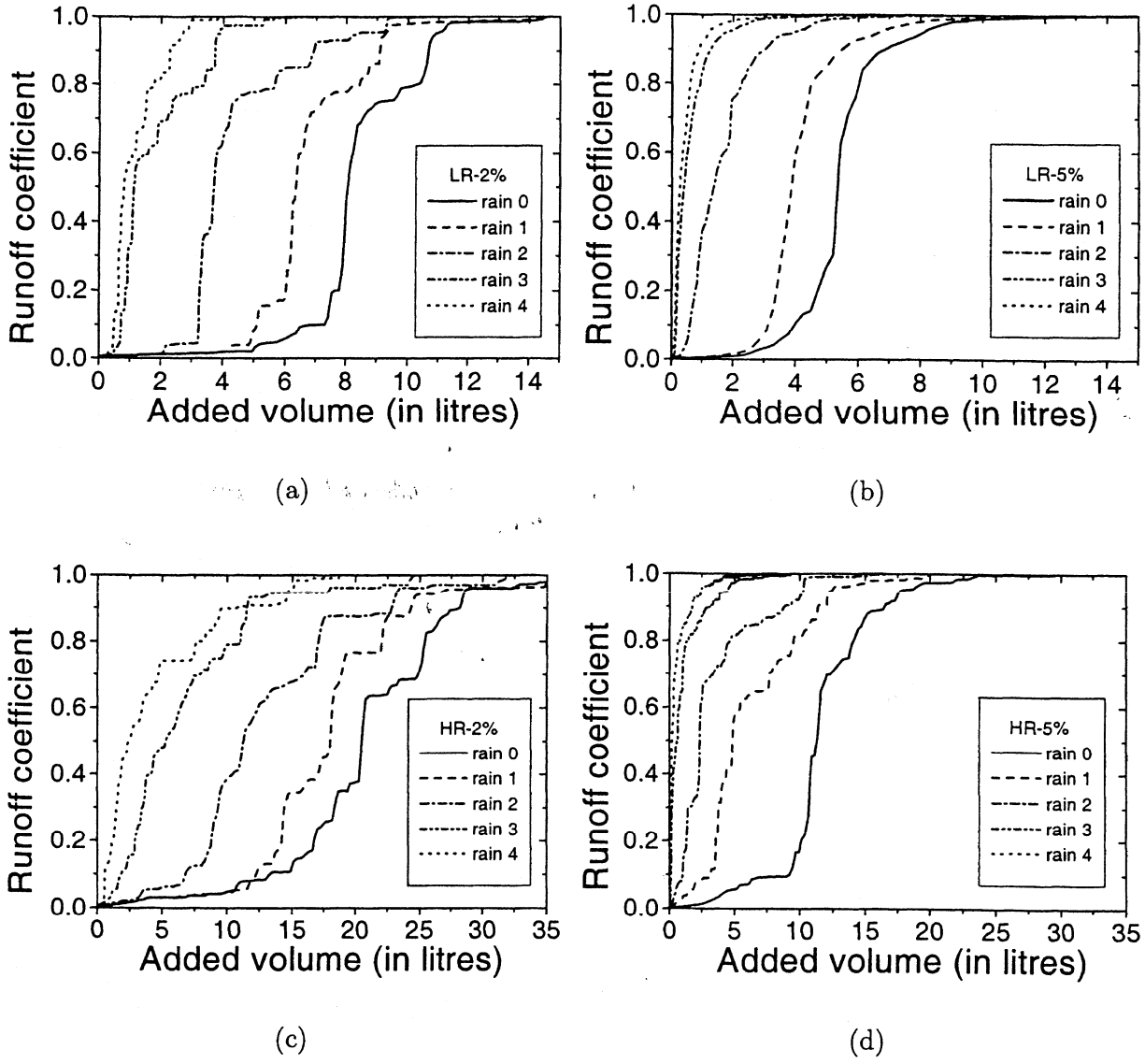

Figure 5.5: Runoff coefficient calculated from conditioned-walker model as functions of on added water for treatments: (a) LR-2%; (b) LR-5%; (c) HR-2%; and (d) HR-5%.

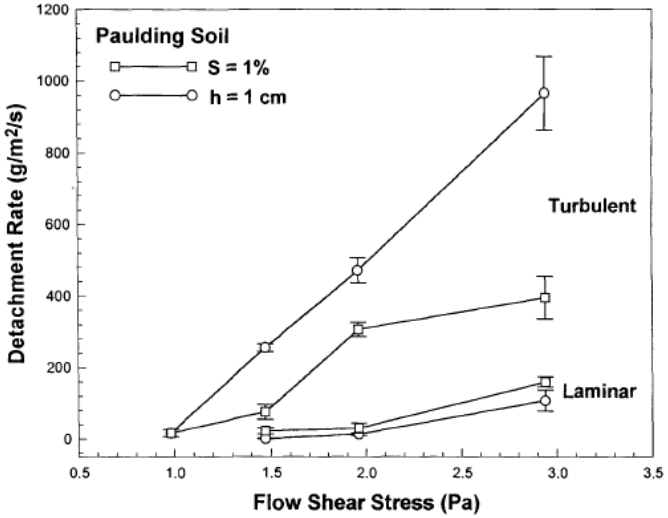

Fig. 1. Detachment rate vs. flow shear stress for turbulent and laminar flow conditions with (i) constant bed slope (S = 1%) and variable flow depth, and also (ii) constant flow depth (h = 1 cm) and variable bed slope for the Paulding soil. Error bars represent 95% confidence interval.

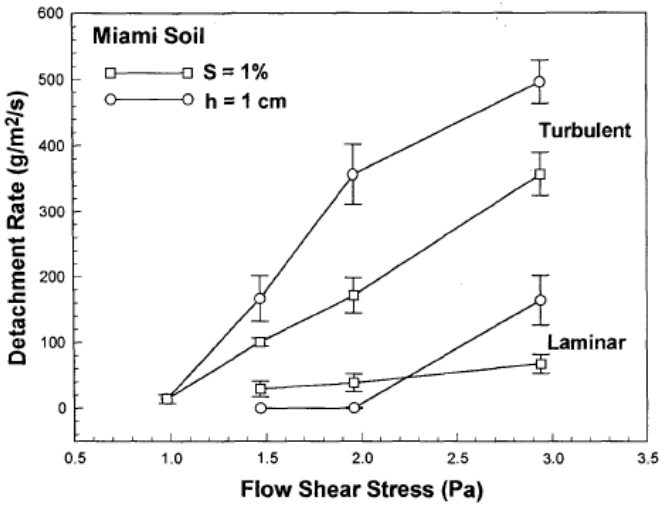

Fig. 2. Detachment rate vs. flow shear stress for turbulent and laminar flow conditions with (i) constant bed slope (S = 1%) and variable flow depth, and also (ii) constant flow depth (h = 1 cm) and variable bed slope for the Miami soil. Error bars represent 95% confidence interval.

Detachment by "Turbulent Bursts"

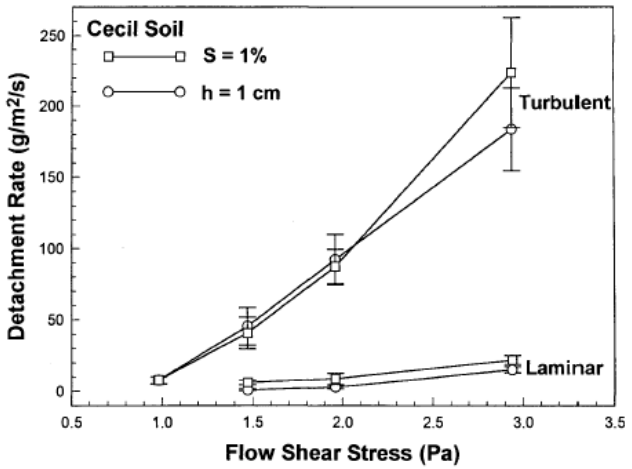

Fig. 3. Detachment rate vs. flow shear stress for turbulent and laminar flow conditions with (i) constant bed slope (S = 1%) and variable flow depth, and also (ii) constant flow depth (h = 1 cm) and variable bed slope for the Cecil soil. Error bars represent 95% confidence interval.

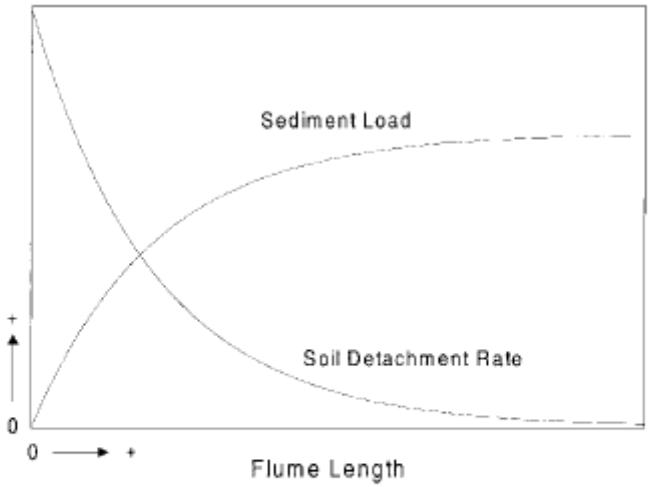

Fig. 1. Schematic diagram of theoretical results for the case of a first-order relationship between sediment load and local detachment rate in a rill. This example is for the case of uniform bed slope, constant and uniform flow rate, and no introduction of sediment from the upper end or sides of the rills.

Helming et al. (1998)

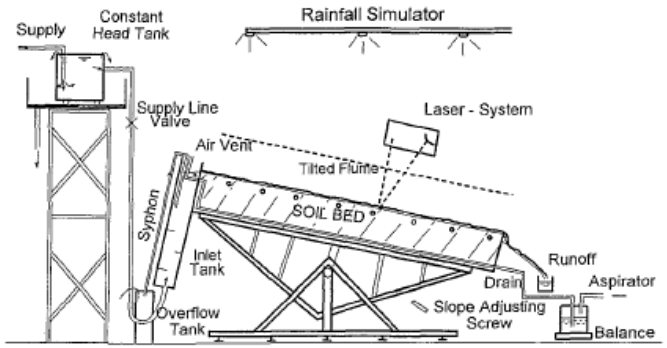

Fig. 1. A schematic diagram of the adjustable flume with rainfall simulator, laser microrelief meter, and drainage system.

Table 2. Total runoff for the four successive rainstorms at three surface conditions and three slope steepnesses.

	Rough	Medium	Smooth
	mm		
	8% slope steepness		
Rain 1, 60 mm h^{-1}	15.8	16.2	12.6
Rain 2, 45 mm h^{-1}	30.2	30.6	23.8
Rain 3, 30 mm h^{-1}	34.2	33.8	29.3
Rain 4, 15 mm h^{-1}	30.2	28.4	28.4
Total	110.4	109.0	94.1

Table 3. Total soil loss for the four successive rainstorms at three surface conditions and three slope steepness.

	Rough	Medium	Smooth
	kg m^{-2}		
	8% slope steepness		
Rain 1, 60 mm h^{-1}	0.54	0.47	0.07
Rain 2, 45 mm h^{-1}	1.13	1.27	0.35
Rain 3, 30 mm h^{-1}	1.11	0.85	0.63
Rain 4, 15 mm h^{-1}	0.53	0.36	0.36
Total	3.31	2.95	1.41

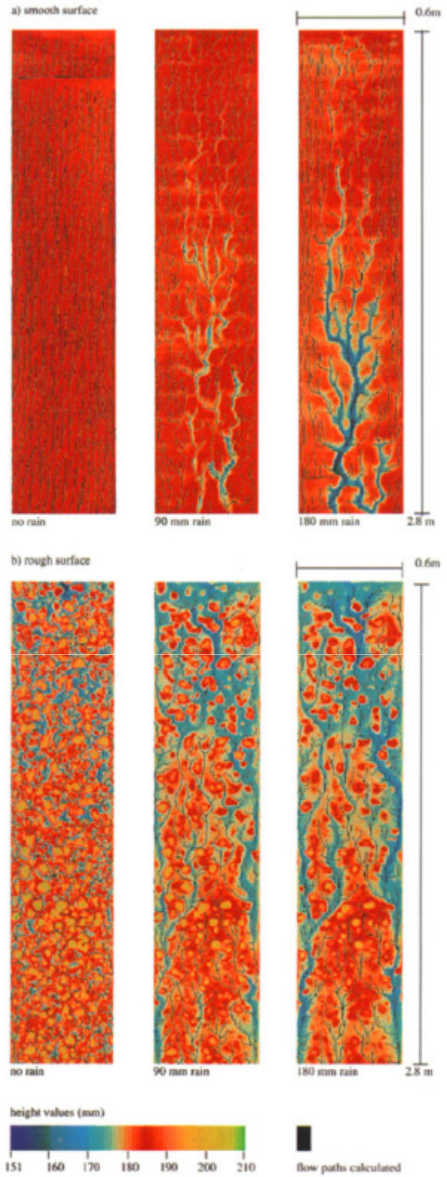

Fig. 4. Runoff flow paths and colored representations of soil surface topography derived from laser microrelief measurements for the initial situation (left), after two rainstorms and a total of 90 mm of rain (middle), and after four rainstorms with a total of 180 mm of rain (right) for (a) a smooth surface condition, and (b) a rough surface condition. Pixel size was 3 by 3 mm. The flow direction is downward.